Electro-optics of perovskite solar cells

Qianqian Lin, Ardalan Armin, Ravi Chandra Raju Nagiri, Paul L. Burn* and Paul Meredith*

Organohalide-perovskite solar cells have emerged as a leading next-generation photovoltaic technology. However, despite surging efficiencies, many questions remain unanswered regarding the mechanisms of operation. Here we report a detailed study of the electro-optics of efficient $CH_3NH_3PbI_3$-perovskite-only planar devices. We report the dielectric constants over a large frequency range. Importantly, we found the real part of the static dielectric constant to be ~70, from which we estimate the exciton-binding energy to be of order 2 meV, which strongly indicates a non-excitonic mechanism. Also, Jonscher's Law behaviour was consistent with the perovskite having ionic character. Accurate knowledge of the cell's optical constants allowed improved modelling and design, and using this information we fabricated an optimized device with an efficiency of 16.5%. The optimized devices have ~100% spectrally flat internal quantum efficiencies and minimal bimolecular recombination. These findings establish systematic design rules to achieve silicon-like efficiencies in simple perovskite solar cells.

Organometallic halide perovskite solar cells have recently emerged as possibly the leading low-cost low-embedded energy photovoltaic technology[1,2]. Progress has been startling since the pioneering work of Kojima et al.[3], who achieved a power conversion efficiency (PCE) of 3.8% using the perovskite component as a visible sensitizer in a dye-sensitized solar cell. During 2014 there have been multiple demonstrations of cells with efficiencies >16%[4,5], along with predictions of a "straightforward path to well above 20%"[1]. The lead-candidate perovskites are based on lead ($CH_3NH_3PbI_{3-x}Cl_x$ with x varying from 0 to 3) with materials that are, to a lesser or greater extent, amenable to solution processing or evaporation[6,7]. Furthermore, a range of device strategies yields high efficiencies: regular[6] and inverted electrical geometries[8], with[6,9,10] or without mesoporous oxide supports[7,8] and using a variety of transport layers[4,11].

Possibly the simplest manifestation of a perovskite solar cell was reported by Malinkiewicz et al.[11] who demonstrated a PCE of 12% in a sandwich of evaporated $CH_3NH_3PbI_3$ between two ultrathin (~10 nm) organic charge-transport layers, polyTPD (poly(N,N'-bis (4-n-butylphenyl)-N,N'-bis(phenyl)benzidine)) and PCBM ((6,6)-phenyl-C61-butyric acid methyl ester). The polyTPD was considered to act as a hole-transporting layer (HTL) at the anode, and the PCBM likewise as an electron-transporting layer (ETL) at the cathode[11]. This structure is electrically inverted with respect to the regular configuration that characterizes most high-efficiency oxide-containing systems and, apart from its simplicity, has the added advantage of low-temperature processing. A PCE >10% is even more remarkable considering the junction was <300 nm thick and an open-circuit voltage of 1.05 V suggests minimal recombination losses and very efficient electron and hole extraction at the electrodes.

This simple planar junction device also highlights an important mechanistic question: clearly the perovskite layer is acting as the light absorber, but how are free carriers generated? Is the system excitonic, like an organic solar cell, which requires a heterojunction interface to separate the electron–hole pair, or do photoexcitations spontaneously dissociate into free carriers in the bulk of the junction, akin to inorganic solar cells? This has been a matter of intense debate, with the various measurements suggesting that exciton-binding energies in perovskites are <50 meV (ref. 12), that

ultrafast interfacial charge-transfer dynamics occur[13] and that the materials have electron- and hole-diffusion lengths between 100 nm and a micron[14,15]. Collectively, these observations point to perovskite solar cells being predominantly non-excitonic. However, continued discussions of the need for n- and p-type electron- and hole-accepting components[7,16], perovskite-photoluminescence quenching in the presence of p- and n-type quenchers[15] and low-temperature signatures of a Wannier–Mott exciton[12] provide continuing uncertainty in this regard. Furthermore, much of our solid-state physics understanding of these perovskites can be traced back to the pioneering work of Ishihara, Hirasawa, Miura and co-workers in the 1990s, who studied lead-based perovskite crystals[17–19]. This includes the first estimates of the exciton-binding energy (E_B), effective masses and, critically, the high-frequency dielectric constants from optical measurements ($\varepsilon = 6.5$)[17,20]. In particular, this high-frequency ε has been routinely, and potentially erroneously, used to determine important material parameters[12,20].

In this article we address several of these important mechanistic issues. Using a simple $CH_3NH_3PbI_3$-perovskite planar junction with ultrathin n- and p-type organic interlayers that act to modify the electrode work functions, we examine and explain critical aspects of the electro-optics of perovskite solar cells. We report accurate optical constants (n, k), map the high- and low-frequency dielectric constants (ε' and ε'') and calculate E_B. Optical cavity modelling based on these n and k values is used to optimize the solar-cell structure and determine the internal quantum efficiency (IQE).

Perovskite structure and ultrathin *p*-type transport layers. We prepared $CH_3NH_3PbI_3$-perovskite junctions on a range of ultrathin (<10 nm) p-type polymeric organic semiconductors commonly used in organic solar cells, including DPP-DTT poly(2,5-(2-octyldodecyl)-3,6-diketopyrrolopyrrole-*alt*-5,5-(2′,5′-di (thien-2-yl)thieno[3,2-b]thiophene), PCDTBT (poly(N-9′-heptadecanyl-2,7-carbazole-*alt*-5,5-(4′,7′-di(thien-2-yl)-2′,1′,3′-benzothiadiazole))), P3HT (poly(3-n-hexylthiophene)) and PCPDTBT (poly (2,6-(4,4-bis(2-ethylhexyl)-4H-cyclopenta[2,1-b;3,4-b′]dithiophene)-*alt*-4′,7′-(2′,1′,3′-benzothiadiazole))) (Fig. 1a). The polymers were chosen based on their ionization potentials (IPs) (Fig. 1b) to modify the work function at the interface with the ITO/PEDOT:
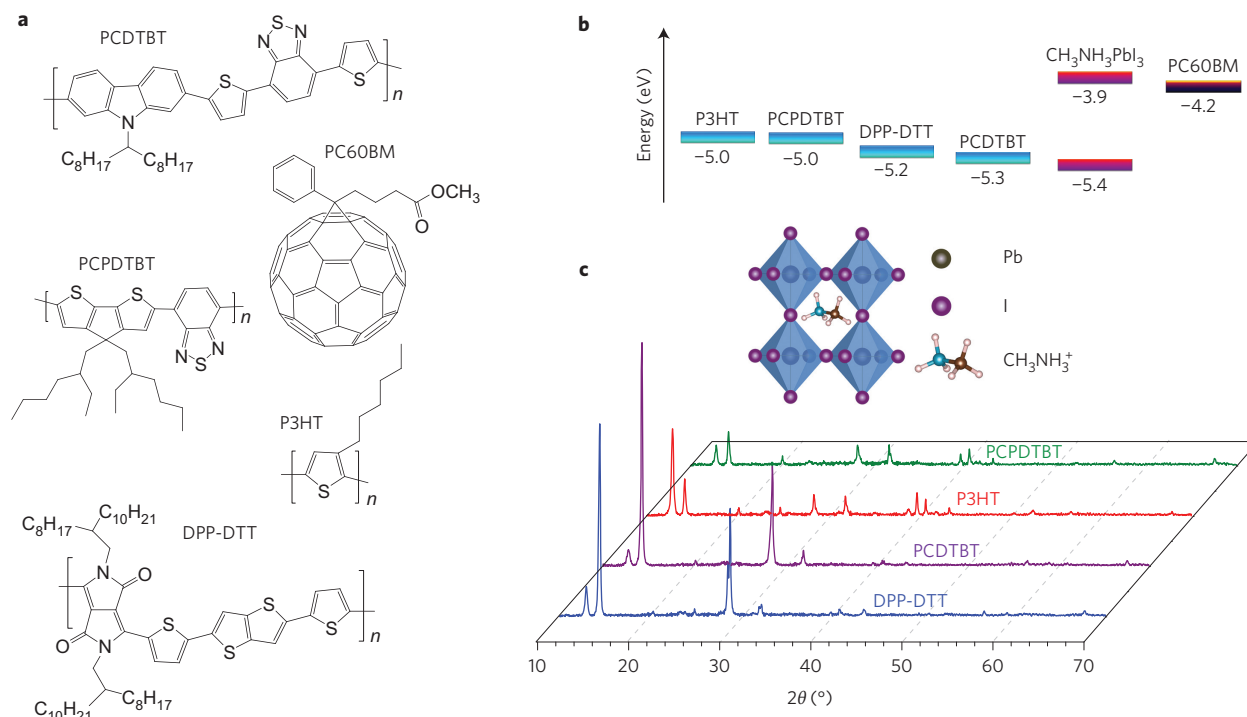
Centre for Organic Photonics & Electronics, School of Chemistry and Molecular Biosciences and School of Mathematics and Physics, The University of Queensland, St Lucia Campus, Brisbane 4072, Australia. *e-mail: p.burn2@uq.edu.au; meredith@physics.uq.edu.au

Figure 1 | Materials and their properties used in the CH₃NH₃PbI₃ non-oxide perovskite solar cells. a, Chemical structures of the polymer interlayers: PCDTBT, PCPDTBT, P3HT, DPP-DTT and PC60BM. **b**, Schematic illustration of the energy levels of CH₃NH₃PbI₃ perovskite (conduction and valence bands[11]), PC60BM 'electron affinity' and *p*-type polymer interlayer ionization potential from the photoelectron spectroscopy in air. **c**, XRD spectra of CH₃NH₃PbI₃-perovskite films grown on different polymer interlayers via thermal evaporation. The inset is the schematic crystal structure of CH₃NH₃PbI₃ perovskite.

PSS (indium tin oxide/poly(3,4-ethylenedioxythiophene):poly (styrene sulfonate)) transparent conducting anode. Thin *n*- or *p*-type interlayers at the cathode or anode are often termed electron- or hole-transport layers (ETLs or HTLs, respectively) and assist in efficient carrier extraction by reducing the electrode-junction potential barrier. However, strictly speaking, if these layers are thinner than the tunnelling distance (as they are in our case), then they do not mediate transport. Hence we refer to the polymers as *p*-type interlayers and the equivalent PC60BM ([6,6]-phenyl-C_{61}-butyric acid methyl ester) at the cathode as an *n*-type interlayer.

Returning to the device fabrication, the CH₃NH₃PbI₃ was vacuum deposited by coevaporation of methyl ammonium iodide (MAI) and lead iodide (PbI₂) (see the Supplementary Information). The structure of the resultant perovskite film was found to be dependent on the *p*-type polymer interlayer used. X-ray diffraction (XRD) spectra of perovskite layers grown on the interlayers are shown in Fig. 1c. High-quality crystals of CH₃NH₃PbI₃ were found to form on PCDTBT and, to a lesser extent, on DPP-DTT, as evidenced by very sharp peaks at 14.27° and 28.60° that correspond to the typical tetragonal crystal structure of the perovskite in the (110) and (220) planes[7]. The perovskite films grown on P3HT and PCPDTBT had lower crystallinity with more-predominant PbI₂ features (12.78° peak)[6]. This structural evidence is supported by optical absorption spectra shown in Supplementary Fig. 1—the films grown on PCDTBT and DPP-DTT have sharp absorption edges (the optical gap) at ~780 nm, characteristic of the CH₃NH₃PbI₃-perovskite structure.

The structural and optical data led us to predict that the PCDTBT interlayer should yield the best solar-cell performance, and this is, indeed, what we found. Prototype devices with the structure glass/ITO/PEDOT:PSS/*p*-type interlayer/perovskite/PC60BM/LiF/Ag were prepared. The perovskite layer was deposited in the same evaporation round for all the interlayers and the other

fabrication conditions were kept constant (see Methods and the Supplementary Information). The perovskite thickness was ~300 nm and the polymer and PC60BM interlayers were <10 nm. Representative current density–voltage (*J*–*V*) curves and external quantum efficiency (EQE) spectra for these prototype cells are shown in Supplementary Fig. 2. The average metrics for these devices are also presented in Supplementary Table 1. The high average open-circuit voltages of the PCDTBT cells ($V_{oc} \simeq 1$ V) are indicative of a good matching between the polymer IP (–5.3 eV) and the perovskite valence-band edge (–5.4 eV). The respectable fill factor (FF ≃ 0.7) and J_{sc} (~16 mA cm⁻²) are probably related to the high crystallinity and quality of the perovskite junction, a fact reinforced by the peak EQEs, which are 70–80%, and the white light PCEs of ~10%.

Having established the effectiveness of PCDTBT and PC60BM as *p*- and *n*-type interlayers, we further optimized the perovskite film quality with respect to the evaporation conditions. Supplementary Fig. 3 shows scanning electron microscopy images of films deposited at different PbI₂ crucible temperatures, 280 °C, 260 °C and 250 °C, and a constant MAI crucible temperature (100 °C), and there is a clear difference in grain size. This is also expected to produce films with slightly different compositions, which is, indeed, what we see from the XRD (Supplementary Fig. 4, (110) and (220) peaks). Based on these data and a further device fabrication study with PCDTBT and PC60BM, 260 °C was chosen as the optimum PbI₂ crucible temperature with our evaporation configuration.

Optical and dielectric constants. To understand the cavity electro-optics of these simple planar perovskite solar cells, the optical constants (refractive index *n* and extinction coefficients *k*) for all layers in the device needed to be determined accurately. To achieve this we used a combination of spectroscopic ellipsometry,
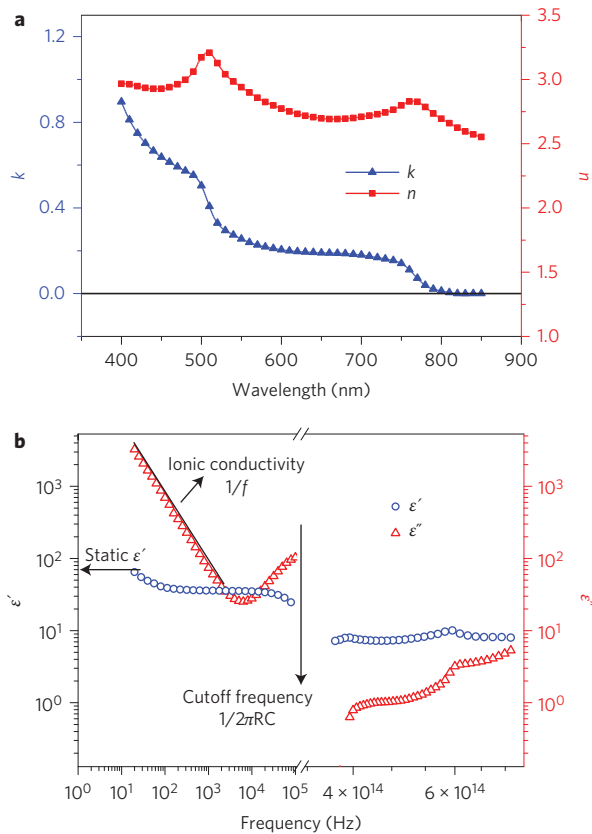
Figure 2 | Optical and dielectric properties of the CH$_3$NH$_3$PbI$_3$ perovskite. **a**, Optical constants of the CH$_3$NH$_3$PbI$_3$: refractive index (n) and extinction coefficient (k), as determined by employing spectroscopic ellipsometry, near-normal incidence reflectance and total transmittance. Three different spectral regions occur: $\lambda > 800$ nm with minimal absorption, 500 nm $< \lambda <$ 800 nm with moderate absorption (comparable with the absorption of typical organic semiconductors) and $\lambda < 500$ nm with the very strong absorption characteristic of PbI$_2$. **b**, Dielectric constants of CH$_3$NH$_3$PbI$_3$, real and imaginary parts, in the optical (high) frequency regime as determined from n, k and low-frequency and static values from impedance analysis and CELIV, respectively. A high static dielectric constant of ~70 is notable. The 1/f behaviour of the imaginary part of the dielectric constant is indicative of the ionic nature of this perovskite.

total transmittance and near-normal incidence reflectance measurements[21]. This is a non-trivial exercise for materials, such as perovskites, that show strong dispersion in both n and k. Our methodology is outlined in Methods and in the flowchart of Supplementary Fig. 5, and involves an iterative self-consistency check that uses an adapted form of the Kramers–Kronig relationship[22]. Figure 2a presents n and k for CH$_3$NH$_3$PbI$_3$ films evaporated under optimum conditions (260 °C with PbI$_2$ and 100 °C with MAI) on PCDTBT. Optimized solar cells were prepared at the same time and tested to ensure the optical constants were measured on device-relevant material. We believe these to be the most-accurate optical constants yet reported for CH$_3$NH$_3$PbI$_3$ for reasons that will become evident below[23]. It is interesting that k (which is a dimensionless representation of the absorption coefficient) shows two sharp edges with onsets at 500 nm and 750 nm: the former is reminiscent of PbI$_2$ and the latter of the optical gap of the perovskite.

These n and k values can be used to calculate the real (ε') and imaginary (ε'') parts of the dielectric constant in the optical frequency range, which are shown in Fig. 2b. The high quality of our evaporated perovskite films also allowed us to measure ε' and ε''

in the low-frequency regime from 20 Hz to ~40 kHz (the upper limit being defined by the resistor–capacitor (RC) characteristic time of the measurement circuit of ~4 μs). This is also shown in Fig. 2b and is augmented by a static measurement using the charge extraction by linearly increasing voltage (CELIV) technique (also shown in Supplementary Fig. 6)[24]. We find ε' in the kilohertz regime to be ~35, in agreement with recent density functional theory (DFT) calculations[25] and pelletized perovskite powders[26]. Of more significance is ε'_{static}, which is ~70—substantially higher than previously thought. The origin of this high static value can be seen in ε'', which shows 1/f behaviour between 20 Hz and 3 kHz, a phenomenon known as 'Jonscher's Law' and a reliable indicator of ionic character[27]. This observation is also consistent with predictions of a ferroelectric molecular domain structure by *ab initio* molecular dynamics simulations[28].

The optical frequency ε' has been used by several authors to calculate important properties of the perovskites[17,18,20]. This is understandable because in many inorganic semiconductors (for example, Si, GaAs and CdTe) the difference between the static and high-frequency values is not large[29]. However, given the data presented in Fig. 2b this is clearly not appropriate for CH$_3$NH$_3$PbI$_3$. The use of the static dielectric constant versus the optical frequency dielectric constant in the Wannier–Mott model is a matter of some debate in the literature[30]. However, given the large exciton radius compared to the lattice constant in perovskites, in this case the static rather than optical frequency value must be used to calculate the exciton-binding energy[31]. More explanation is provided in the Methods in this regard. Following the magneto-optical approaches of Taguchi *et al.*[32], Hirasawa *et al.*[18] and Tanaka *et al.*[20], which are derived from the static solution of a perturbed Wannier–Mott exciton Hamiltonian in a weak magnetic field, we calculated the binding energy using $\varepsilon'_{static} = 70$ and found $E_B \approx 1.7$–2.1 meV (see Methods). D'Innocenzo *et al.*[12] recently estimated E_B in a mixed-halide perovskite crystal to have an upper bound of 50 meV, and Hirasawa *et al.* similarly calculated a value of 38 meV based on $\varepsilon' = 6.5$ (ref. 17). Hence, our value of $E_B \approx 2$ meV is much smaller than previously reported from experimental observations, although not inconsistent with these upper bounds. However, from DFT calculations that assumed bare band effective masses, Frost *et al.*[33] recently predicted an even lower binding energy of 0.7 meV. They also recently suggested[28] that, taking electron–phonon couplings into account, the binding energy could be larger and hence closer to the values that we report here. Irrespective of the exact value, such a low E_B (examples are Si, 15.0 meV; GaAs, 4.2 meV; CdTe, 10.5 meV (ref. 34)) dictates that perovskite solar cells should be predominantly non-excitonic at room temperature. It also has broader implications for the operation of perovskite solar cells—for example, one expects minimal bimolecular recombination because the electron–hole interaction cross-section is proportional to 1/ε'^2_{static}. We return to this important point later in the paper. Finally, we used diamagnetic coefficients from Hirasawa *et al.*[17] as the upper ($c_0 = 2.7 \times 10^{-6}$ eV T^{-2}) and from Tanaka *et al.*[20] as the lower ($c_0 = 1.35 \times 10^{-6}$ eV T^{-2}) limits. From the Wannier analysis it emerges that E_B is relatively insensitive to c_0 (power 1/3 dependence), but it is proportional to the ε'_{static} to the power –4/3; that is, it is strongly dependent on ε'_{static}.

Cavity modelling and optimization of perovskite solar-cell performance. Accurate knowledge of n and k for all layers in the solar cell allows one to perform cavity modelling (transfer-matrix analysis) and predict the optical-field distribution in the device[35,36]. Assuming an IQE of 100%, it is possible to determine how the short-circuit current varies as a function of the cell geometry and, in particular, the perovskite-junction thickness. Such a process has been used to optimize organic solar cells successfully, and all the optical constants of non-active layers
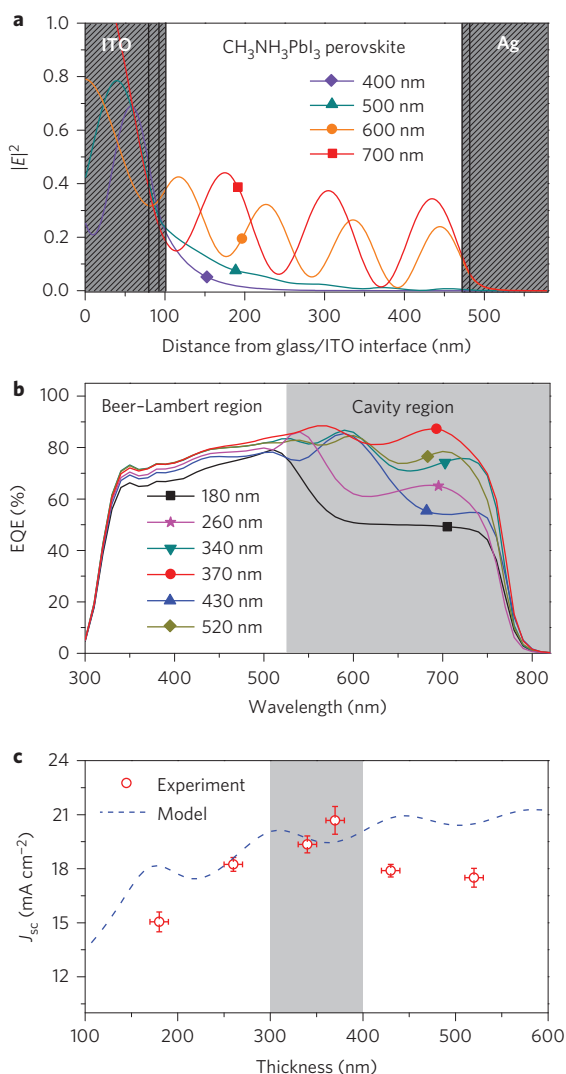
Figure 3 | Electro-optical modelling of perovskite solar cells. a, Optical-field distribution in a CH₃NH₃PbI₃-perovskite device for four wavelengths: for $\lambda < 500$ nm the optical-field distribution follows the Beer–Lambert law and no optical field reaches to the back electrode as a result of the high absorption coefficient. In such cases the absorption is saturated and no optical interference occurs. For $\lambda > 500$ nm the optical field is governed by low-finesse cavity interference. **b**, EQE spectra of devices with different CH₃NH₃PbI₃-layer thicknesses. For $\lambda < 500$ nm there is minimal influence of the film thickness, but for $\lambda > 500$ nm the EQE is strongly thickness dependent because of the optical interference. **c**, Comparison of experimental short-circuit current density J_{sc} and modelled J_{sc} (assuming IQE is 100%). It was predicted that by increasing the thickness, the photocurrent density would reach a maximum of ~21 mA cm⁻² at an active layer thickness of 350 nm. This was confirmed experimentally. As a result of morphological effects, the maximum photocurrent density falls off at thicker active layers.

required for the analysis (glass, ITO, PEDOT:PSS, PCDTBT, PC60BM and Ag) are shown in Supplementary Fig. 7. In Fig. 3a we present an example simulation for the optimized structure, glass/ITO (80 nm)/PEDOT:PSS (15 nm)/PCDTBT (5 nm)/perovskite (350 nm)/PC60BM (10 nm)/Ag (100 nm) for four incident wavelengths. Immediately, we see two different regimes of behaviour: (1) for $\lambda < 500$ nm the cavity operates in the Beer–Lambert regime (exponential dependence of the field on propagation distance) and (2) for $\lambda > 500$ nm the cavity operates
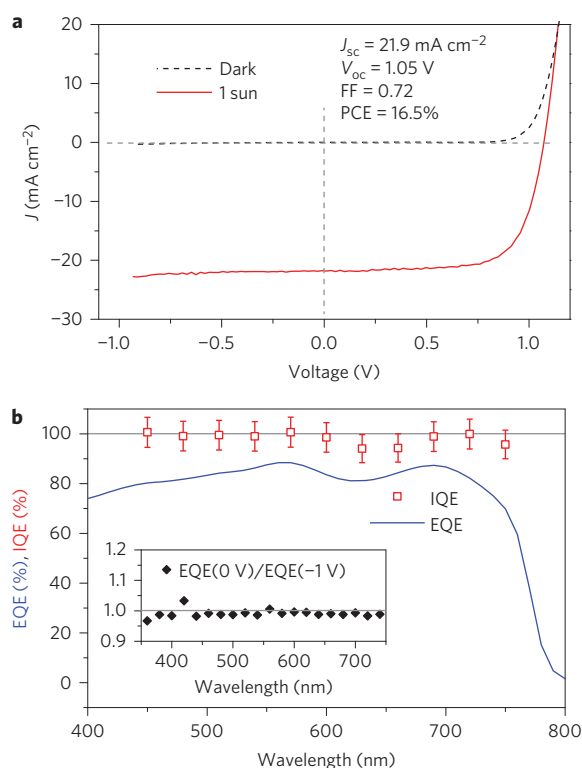

Figure 4 | Solar-cell performance of the 'hero' CH₃NH₃PbI₃ perovskite. a, Dark and light J–V curves (scan from –1 V to 1.2 V with a scan rate of 0.1 V s⁻¹) of the best-performing CH₃NH₃PbI₃-perovskite solar cell optimized based on Fig. 3. **b**, EQE and IQE spectra of a corresponding device. The IQE is spectrally flat and ~100% to within the error of measurement (±5%). The inset shows the ratio of EQE measured without bias and with a –1 V reverse bias and shows that carrier extraction is essentially lossless.

in the low-finesse thin-film interference regime[36]. Simplistically, the cavity is strongly absorbing in the former regime and weakly absorbing in the latter. Hence, one can predict that the EQE should be fully saturated even for thin perovskite junctions (<150 nm) for $\lambda < 500$ nm.

This is a very important insight and dictates that optimization must therefore focus on maximizing photon harvesting between 500 nm and 800 nm, where the EQE is strongly dependent on the perovskite-junction thickness. This prediction is confirmed by the experimental data shown in Fig. 3b in which we plot the EQE of various devices of different junction thicknesses. Also, the n and p interlayer thicknesses have a subtle but important impact on the maximum J_{sc}. We show this effect in Supplementary Fig. 8 simulated for a 350 nm perovskite device—PCDTBT absorbs in the visible and the interlayer must therefore be as thin as possible, preferably ~5 nm. The system is more tolerant of the PC60BM interlayer thickness, but likewise the thinner the better. In Fig. 3c we bring all of this understanding together and plot the simulated J_{sc} as a function of junction thickness (assuming 100% IQE) in an optimized configuration. We predict the maximum possible photocurrent to be near 21 mA cm⁻². We also know that for our deposition process the perovskite film quality becomes compromised when it is thicker than ~400 nm (shorting defects that arise from large crystals). Hence we predict a 'sweet spot' at ~350 nm and the experimental data from a detailed thickness-dependent study confirms this to be the case. The relatively good agreement between simulations and experiment in the thickness regime where the FF is not compromised by the film structure underlines the validity of our optical constants, which we estimate to be accurate to within 5%.

Table 1 | CH₃NH₃PbI₃-perovskite solar-cell performance statistics.

	J_{sc} (mA cm⁻²)	V_{oc} (V)	FF	PCE (%)
180 nm	15.1 ± 0.6	1.05 ± 0.00	0.74 ± 0.06	11.2 ± 0.7
260 nm	18.2 ± 0.4	1.04 ± 0.01	0.69 ± 0.03	13.1 ± 0.6
340 nm	19.4 ± 0.5	1.05 ± 0.01	0.73 ± 0.02	14.6 ± 0.4
370 nm	20.7 ± 0.8	1.05 ± 0.01	0.71 ± 0.02	15.2 ± 1.1
430 nm	17.9 ± 0.4	1.05 ± 0.01	0.73 ± 0.03	13.7 ± 0.4
520 nm	17.5 ± 0.5	1.03 ± 0.01	0.61 ± 0.04	10.9 ± 1.1

These are based on 12 devices for each round of optimized device fabrication, with a scan from −1 V to 1.2 V and a scan rate of 0.1 V s⁻¹ as a function of perovskite-junction thickness.

Figure 4a shows the white-light air mass 1.5 global (AM 1.5G) J–V curve for our 'hero' device (perovskite-layer thickness 370 nm) with a PCE of 16.5%, FF = 0.72, V_{oc} = 1.05 V and J_{sc} = 21.9 mA cm⁻². Statistics for all the devices of Fig. 3c are shown in Table 1. The integrated EQE currents also agree within 10% of the measured white-light J_{sc}. This result is by far the highest efficiency of a non-oxide perovskite-only cell yet reported. Recently, several groups have demonstrated severe J–V hysteresis in perovskite solar cells, which makes accurate PCE measurements problematic[37]. However, in line with other reports of simple planar devices that employ effective HTLs and ETLs[38,39], we observe no hysteresis over a range of J–V scan rates. Data for typical optimized cells as-made and encapsulated are provided in Supplementary Fig. 9. These findings may indicate that surface-trap defects play a role in the hysteresis, but more evidence is required to be definitive in this regard. Devices encapsulated for the hysteresis study were also tested periodically over a period more than four months (in total more than 30 times with more than eight hours of 1 sun illumination). Supplementary Fig. 10 shows the stability of key performance metrics over this period of time and we observed a ~10% degradation in PCE.

Finally, we present in Fig. 4b the IQE of the 16.5% cell. The IQE was determined using an analysis recently reported[35,36] that requires measurement of the EQE and accurate calculation of the junction absorption from near-normal incidence reflectance measurements, transfer-matrix modelling and assessment of all non-active layer parasitic absorbances. The IQE between 450 nm and 750 nm is spectrally flat and equal to 100% within the error of the measurement[36]. This observation rules out energy-dependent charge generation and the influence of hot exciton or carrier effects, and confirms the near-unity charge generation and collection efficiency of these perovskite solar cells. The inset in Fig. 4b shows a comparison of the EQE at the short circuit and −1 V (presented as a ratio). This also confirms the almost perfect charge-collection efficiency, which suggests minimal bimolecular recombination. In comparison with organic solar cells, for a junction thickness of 300 nm the high dielectric constant means that the capacitance per unit area in a perovskite solar cell is around 20 times larger. Accordingly, a large amount of charge can be accommodated without the onset of space-charge limitations, so bimolecular recombination should only emerge at very high illumination intensities. We showed that the current density versus input irradiance is linear out to greater than 1 sun equivalent power (Supplementary Fig. 11), which adds further weight to this assertion. This confirms a low bimolecular recombination under normal operating conditions.

Conclusion

In this article we present a comprehensive analysis of the electro-optics of perovskite solar cells. Using a simple CH₃NH₃PbI₃-perovskite planar junction with ultrathin n- and p-type organic work-function modifying interlayers, we examine and explain the cavity optics and present accurate optical constants (n, k). We demonstrate how the p-type interlayer affects the perovskite film composition, structure and open-circuit voltage. Using the optical constants as a starting point, we also present a comprehensive map of the low- and high-frequency dielectric constants and show the static ε'_{static} (the relevant quantity for calculating the exciton-binding energy in the Wannier–Mott regime) to be ~70, much higher than previously thought. This leads to a new estimate of the exciton-binding energy of ~2 meV, which confirms that these systems are predominantly non-excitonic. We also present evidence of the ionic nature of CH₃NH₃PbI₃, which could explain the high static dielectric constant. Armed with this optical and electrical data we use transfer-matrix simulations to model the expected short-circuit current density as a function of junction structure. Experiment and modelling are in good agreement and both confirm that these perovskite solar cells operate in two distinct cavity regimes: within the Beer–Lambert limit for λ < 500 nm, and as low-finesse interference cavities for λ > 500 nm. This insight simplifies the junction-thickness optimization, which requires maximizing photon harvesting in the interference spectral regime. We arrive at an optimized device geometry that delivers a maximum PCE at AM 1.5G of 16.5% (hysteresis free). This is by far the highest PCE reported for a non-oxide, perovskite-only solar cell. The 'hero' device has an IQE of ~100% that is spectrally flat from 450 nm to 750 nm, which rules out any hot exciton or hot carrier effects over that range. Moreover, these devices demonstrate a strongly suppressed recombination behaviour (minimal bimolecular recombination) and near-unity charge generation and extraction. The properties that we report were determined for materials totally representative of those used in high-efficiency devices. Our findings establish electro-optic design rules that we believe are generic for perovskite solar cells and provide further insight into how these systems work as photovoltaic materials. Furthermore, a detailed understanding of the cavity optics will be required for the efficient design of tandem structures.

Methods

Details of materials, the preparation of MAI, device fabrication and dual-source evaporation are given in the Supplementary Information.

Characterization. Optical absorption spectra were collected using a Varian Cary 5000 ultraviolet–visible–near infrared spectrophotometer in the range 300–1,200 nm. All films for absorbance measurements were representative of the in-device structure. IPs were determined using photoelectron spectroscopy in air on thin films on quartz. The crystalline nature of the films was characterized by XRD. All XRD spectra were obtained on a Bruker Advance D8 X-ray diffractometer equipped with a LynxEye detector, Cu tube (CuKα = 1.5418 Å) and operated at 40 kV with a 2θ scan range of 10–70°. The surface morphology and cross-sectional images of the devices were observed using a Jeol JSM-7100F field-emission scanning electron microscope with an accelerating voltage of 1 keV. Film thicknesses were determined using a surface profilometer (Veeco Dektak 150). The extinction coefficient k was calculated from the total transmittance acquired by an integrating sphere on a Perkin-Elmer Lambda 950 spectrophotometer accurately base-lined with a reference glass slab and near-normal incidence reflectance measurements obtained using a FilmTek 2000M TSV thin-film measurement system. The films for these measurements were encapsulated using spun-cast Cytop to prevent degradation over the measurement period. The real part of the refractive index (n) was determined from a transformation of the Kramers–Kronig relation from the extinction coefficient (k) and base-lined with n (λ > 800 nm) extracted from the spectroscopic ellipsometry data collected on a J. A. Woollam VUV-VASE ellipsometer. Dielectric constants in the high-frequency regime (~10¹⁴ Hz) were converted from the optical constants (n and k). The dielectric constants at 20 Hz to ~10⁵ Hz were measured using an Agilent E4980A LCR meter. The RC characteristic time for the circuit was ~4 µs, which corresponds to a frequency limit of <40 KHz. The static dielectric constant was measured by the CELIV technique, as explained in detail in Armin et al.[24].

Device-performance measurement. The J–V characteristics were obtained using a Keithley 2400 source and measurement unit in a connected four-wire configuration in the dark and under 1 sun illumination (AM 1.5G, ~100 mW cm⁻², without a mask) with a scan speed of 0.1 V s⁻¹. The solar simulator (Abet Triple-A, Abet Technologies) was calibrated with a National Renewable Energy Laboratory (NREL)-certified standard 2 cm × 2 cm silicon photodiode with a KG5 filter. Within the illumination area of 5 cm × 5 cm, the variation of the light intensity was below 3% (measured with a standard photodiode). All the device measurements were undertaken in an MBraun nitrogen glovebox (O₂ < 0.1 ppm, H₂O < 0.1 ppm).

EQE spectra and the near-normal incidence reflectance of the devices were recorded by a PV Measurements Inc. QEX7 set-up, which was calibrated by a NREL-certified photodiode without light bias. Integrated EQE currents were cross-checked for consistency with the white-light short-circuit current and found to be within 10%. Statistics of device performance were based on 12 devices (0.2 cm² area) for each round of device fabrication unless otherwise stated. Intensity-dependent photocurrents were measured by a second harmonic Nd:YAG laser (Laserver) as the illumination source that operated continuously at 532 nm with a series of neutral density filters purchased from Thorlabs and Holmarc. The light intensity was calibrated by a standard photodiode simultaneously to compensate for intensity fluctuations and the current response was recorded by an Agilent B1500A semiconductor analyser.

Transfer-matrix simulations. The optical-field distributions and short-circuit current under AM 1.5G solar illumination were modelled using a Matlab code developed by Burkhard et al.[35] and based on a transfer-matrix method described by Pettersson et al.[40].

Calculation of the exciton-binding energy. For an electron and hole pair in a semiconductor (compared with the hydrogen atom), the Coulomb interaction is effectively screened by the static dielectric constant ϵ'_{static} and the exciton-binding energy is a modified Rydberg energy given by a static solution to the Wannier equation[41]:

$$E_B = \frac{\mu}{m_0} \frac{1}{\epsilon^2} \frac{m_0 e^4}{2(4\pi\epsilon_0 \hbar)^2} \qquad (1)$$

with μ being the exciton effective mass, m_0 the electron mass, e the unit charge and ϵ_0 the vacuum permittivity. For large separations between the electron and hole in a semiconductor, the crystal can be treated as a homogeneous medium with a static dielectric constant that screens their electric fields[31]. This screening is primarily caused by polarization of the lattice; that is, the excitation of optical phonons. When the electron–hole separation is smaller, the polarization of longitudinal optical phonons cannot respond on the timescale of the electron–hole movement[42]. In this case, the screening can only occur via the polarization of the valence electrons and, as such, the optical frequency dielectric constant is the more-relevant quantity. The exciton radius has been calculated to be 204 Å (ref. 33), a value much larger than the lattice constant[43]. Therefore, the use of the high-frequency constant is not justified, and the static value must be used. To estimate the binding energy, the effective mass is required, which can be evaluated from magneto-absorption measurements based on the theory described by Roth et al.[44]. In the presence of a weak magnetic field B, that is when $\hbar\omega_c \leq E_B$ where ω_c is the cyclotron frequency eB/μ, the Wannier equation can be rewritten with a perturbed Hamiltonian. The first-order Eigen values for such a perturbed Hamiltonian include a diamagnetic energy shift of:

$$\Delta E = \frac{4\pi^2 \hbar^4 \epsilon^2 \epsilon_0^2}{\mu^3 e^2} B^2 = c_0 B^2 \qquad (2)$$

from which the effective mass is calculated, as described by Taguchi et al.[32]. According to the measured dielectric constant shown in Fig. 2b and values for c_0 reported by Hirasawa et al.[17] and Tanaka et al.[20] the effective mass will be $0.6m_0 < \mu < 0.7m_0$, which corresponds to a binding energy of 1.7 meV $< E_B <$ 2.1 meV.

References

1. Service, R. F. Perovskite solar cells keep on surging. *Science* **344,** 458–458 (2014).
2. Burn, P. L. & Meredith, P. The rise of the perovskites: the future of low cost solar photovoltaics. *NPG Asia Mater.* **6,** e79 (2014).
3. Kojima, A., Teshima, K., Shirai, Y. & Miyasaka, T. Organometal halide perovskites as visible-light sensitizers for photovoltaic cells. *J. Am. Chem. Soc.* **131,** 6050–6051 (2009).
4. Jeon, N. J. et al. o-Methoxy substituents in spiro-OMeTAD for efficient inorganic–organic hybrid perovskite solar cells. *J. Am. Chem. Soc.* **136,** 7837–7840 (2014).
5. Zhou, H. et al. Interface engineering of highly efficient perovskite solar cells. *Science* **345,** 542–546 (2014).
6. Burschka, J. et al. Sequential deposition as a route to high-performance perovskite-sensitized solar cells. *Nature* **499,** 316–319 (2013).
7. Liu, M. Z., Johnston, M. B. & Snaith, H. J. Efficient planar heterojunction perovskite solar cells by vapour deposition. *Nature* **501,** 395–398 (2013).
8. Docampo, P., Ball, J. M., Darwich, M., Eperon, G. E. & Snaith, H. J. Efficient organometal trihalide perovskite planar-heterojunction solar cells on flexible polymer substrates. *Nature Commun.* **4,** 2761 (2013).
9. Etgar, L. et al. Mesoscopic CH₃NH₃PbI₃/TiO₂ heterojunction solar cells. *J. Am. Chem. Soc.* **134,** 17396–17399 (2012).
10. Wojciechowski, K., Saliba, M., Leijtens, T., Abate, A. & Snaith, H. Sub 150 °C processed meso-superstructured perovskite solar cells with enhanced efficiency. *Energy Environ. Sci.* **7,** 1142–1147 (2014).
11. Malinkiewicz, O. et al. Perovskite solar cells employing organic charge-transport layers. *Nature Photon.* **8,** 128–132 (2014).
12. D'Innocenzo, V. et al. Excitons versus free charges in organo-lead tri-halide perovskites. *Nature Commun.* **5,** 3586 (2014).
13. Marchioro, A. et al. Unravelling the mechanism of photoinduced charge transfer processes in lead iodide perovskite solar cells. *Nature Photon.* **8,** 250–255 (2014).
14. Lee, M. M., Teuscher, J., Miyasaka, T., Murakami, T. N. & Snaith H. J. Efficient hybrid solar cells based on meso-superstructured organometal halide perovskites. *Science* **338,** 643–647 (2012).
15. Stranks, S. D. et al. Electron-hole diffusion lengths exceeding 1 micrometer in an organometal trihalide perovskite absorber. *Science* **342,** 341–344 (2013).
16. Qin, P. et al. Inorganic hole conductor-based lead halide perovskite solar cells with 12.4% conversion efficiency. *Nature Commun.* **5,** 3834 (2014).
17. Hirasawa, M., Ishihara, T., Goto, T., Uchida, K. & Miura, N. Magnetoabsorption of the lowest exciton in perovskite-type compound (CH₃NH₃)PbI₃. *Physica B* **201,** 427–430 (1994).
18. Hirasawa, M., Ishihara, T. & Goto, T. Exciton features in 0-dimensional, 2-dimensional, and 3-dimensional networks of [PbI₆]⁴⁻ octahedra. *J. Phys. Soc. Jpn* **63,** 3870–3879 (1994).
19. Muljarov, E. A., Tikhodeev, S. G., Gippius, N. A. & Ishihara, T. Excitons in self-organized semiconductor/insulator superlattices: PbI-based perovskite compounds. *Phys. Rev. B* **51,** 14370–14378 (1995).
20. Tanaka, K. et al. Comparative study on the excitons in lead–halide-based perovskite-type crystals CH₃NH₃PbBr₃ and CH₃NH₃PbI₃. *Solid State Commun.* **127,** 619–623 (2003).
21. Pankove, J. I. *Optical Progresses in Semiconductors* (Dover Publications, 2010).
22. Roessler, D. M. Kramers–Kronig analysis of non-normal incidence reflection. *Br. J. Appl. Phys.* **16,** 1359–1366 (1965).
23. Xing, G. et al. Low-temperature solution-processed wavelength-tunable perovskites for lasing. *Nature Mater.* **13,** 476–480 (2014).
24. Armin, A. et al. Doping-induced screening of the built-in-field in organic solar cells: effect on charge transport and recombination. *Adv. Energy Mater.* **3,** 321–327 (2013).
25. Brivio, F., Butler, K. T., Walsh, A. & van Schilfgaarde, M. Relativistic quasiparticle self-consistent electronic structure of hybrid halide perovskite photovoltaic absorbers. *Phys. Rev. B* **89,** 155204 (2014).
26. Onoda-Yamamuro, N., Matsuo, T. & Suga, H. Dielectric study of CH₃NH₃PbX₃ (X = Cl, Br, I). *J. Phys. Chem. Solids* **53,** 935–939 (1992).
27. Jonscher, A. K. Analysis of the alternating current properties of ionic conductors. *J. Mater. Sci.* **13,** 553–562 (1978).
28. Frost, J. M., Butler, K. T. & Walsh, A. Molecular ferroelectric contributions to anomalous hysteresis in hybrid perovskite solar cells. *APL Mater.* **2,** 081506 (2014).
29. Philipp, H. R. & Ehrenreich, H. Optical properties of semiconductors. *Phys. Rev.* **129,** 1550–1560 (1963).
30. Huang, L. Y. & Lambrecht, W. R. Electronic band structure, phonons, and exciton binding energies of halide perovskites CsSnCl₃, CsSnBr₃, and CsSnI₃. *Phys. Rev. B* **88,** 165203 (2013).
31. Madelung, O. *Introduction to Solid-State Theory* Vol. 2 (Springer, 1996).
32. Taguchi, S., Goto, T., Takeda, M. & Kido, G. Magneto-optical effects of the Wannier exciton in a biaxial ZnP crystal. I. *J. Phys. Soc. Jpn* **57,** 3256–3261 (1988).
33. Frost, J. M. et al. Atomistic origins of high-performance in hybrid halide perovskite solar cells. *Nano Lett.* **14,** 2584–2590 (2014).
34. Pelant, I. & Valenta, J. *Luminescence Spectroscopy of Semiconductors* (Oxford Univ. Press, 2012).
35. Burkhard, G. F., Hoke, E. T. & McGehee, M. D. Accounting for interference, scattering, and electrode absorption to make accurate internal quantum efficiency measurements in organic and other thin solar cells. *Adv. Mater.* **22,** 3293–3297 (2010).
36. Armin, A. et al. Quantum efficiency of organic solar cells: electro-optical cavity considerations. *ACS Photon.* **1,** 173–181 (2014).
37. Snaith, H. J. et al. Anomalous hysteresis in perovskite solar cells. *J. Phys. Chem. Lett.* **5,** 1511–1515 (2014).
38. Wang, Q., et al. Large fill-factor bilayer iodine perovskite solar cells fabricated by a low-temperature solution-process. *Energy Environ. Sci.* **7,** 2359–2365 (2014).
39. Malinkiewicz, O. et al. Metal-oxide-free methylammonium lead iodide perovskite-based solar cells: the influence of organic charge transport layers. *Adv. Energy Mater.* **4,** 1400345 (2014).
40. Pettersson, L. A. A., Roman, L. S. & Inganäs, O. Modeling photocurrent action spectra of photovoltaic devices based on organic thin films. *J. Appl. Phys.* **86,** 487–496 (1999).
41. Grundmann, M. *The Physics of Semiconductors* (Springer, 2006).
42. Klingshirn, C. F. *Semiconductor Optics* Vol. 3 (Springer, 2007).

43. Mosconi, E., Amat, A., Nazeeruddin, M. K., Grätzel, M. & De Angelis, F. First-principles modeling of mixed halide organometal perovskites for photovoltaic applications. *J. Phys. Chem. C* **117,** 13902–13913 (2013).
44. Roth, L. M., Lax, B. & Zwerdling, S. Theory of optical magneto-absorption effects in semiconductors. *Phys. Rev.* **114,** 90–103 (1959).

Author contributions

Q.L. synthesized the MAI, prepared perovskite films and performed the basic characterization. Q.L. fabricated the solar-cell devices and Q.L. and A.A. tested them. Q.L., A.A., P.M. and P.L.B. designed the devices and experiments. R.C.R.N. and P.M. performed the spectroscopic ellipsometry and reflectometry and R.C.R.N., P.M. and A.A. fitted the data. A.A. and P.M. carried out the dielectric constant/binding energy analysis. All the authors contributed in writing the manuscript.

Additional information

Supplementary information is available in the online version of the paper. Reprints and permissions information is available online at www.nature.com/reprints. Correspondence and requests for materials should be addressed to P.L.B. and P.M.

Competing financial interests

The authors declare no competing financial interests.